crystals

MDPI

Article

Ultra-Strong High-Temperature Mechanical Properties of an Ultrafine-Grained Eutectic Al-Si Alloy by Mechanical Alloying and Press Forming

Lin Zhang [1,2,†], Chang Xu [1], Zhongkan Ren [2], Jingtao Liu [3], Junchen Zhang [3], Junfeng Zhang [3], Xu Wu [2], Pengfei Ji [2], Youjian Zhang [2], Huaguo Tang [2,4,5,*], Wenjie Zhong [1,2,*], Lin Song [6,*,†] and Zhenlin Yang [1,*]

1 Yantai Research Institute, Harbin Engineering University, No. 145, Nantong Street, Harbin 150001, China; zl15940813332@gmail.com (L.Z.); changxu_1021@163.com (C.X.)
2 Shandong Laboratory of Yantai Advanced Materials and Green Manufacturing, Yantai 264006, China; zhongkanren@163.com (Z.R.); wux@amgm.ac.cn (X.W.); jpf_jpf_jpf@163.com (P.J.); yjzhang@ytu.edu.cn (Y.Z.)
3 Shandong Ludian Line Equipment Co., Ltd., Yantai 265301, China; liujingtao@126.com (J.L.); ylm19808@amgm.ac.cn (J.Z.); laotang@amgm.ac.cn (J.Z.)
4 State Key Laboratory of Solid Lubrication, Lanzhou Institute of Chemical Physics, Chinese Academy of Sciences, Lanzhou 730000, China
5 Yantai Huihua Metal Sci. & Tech. Co., Ltd., Yantai 264006, China
6 School of Mechanical Engineering, Shandong University, Jinan 250061, China
* Correspondence: laotang@licp.cas.cn (H.T.); zwj15684139786@126.com (W.Z.); songlin@sdu.edu.cn (L.S.); yangzhenlin@hrbeu.edu.cn (Z.Y.)
† These authors contributed equally to this work.

Abstract

A high strength Al-12Si has been prepared through mechanical alloying and press forming without any additional alloy components. The alloy exhibited a high tensile strength of 458 MPa at room temperature and retained excellent tensile properties at elevated temperatures with a UTS of 118 MPa at 350 °C after 1000 h of exposure. Furthermore, after 1000 h of heat exposure testing, the mechanical properties of the alloy showed no significant decrease. X-ray diffraction characterizations indicated that the alloy consists solely of an Al matrix and Si phase. Microstructural characterization through HRTEM revealed that the grain size of the Al matrix was approximately 300 nm, with a high-density of stacking faults present. The grain refinement strengthening and stacking fault strengthening contributed to the alloy's excellent mechanical properties at both room temperature and elevated temperatures.

Keywords: Al-Si alloy; mechanical alloying & press-forming; grain refinement; stacking faults; high-temperature mechanical properties

Check for updates

Academic Editor: Umberto Prisco

Received: 10 February 2026
Revised: 28 February 2026
Accepted: 3 March 2026
Published: 5 March 2026

Copyright: © 2026 by the authors. Licensee MDPI, Basel, Switzerland. This article is an open access article distributed under the terms and conditions of the Creative Commons Attribution (CC BY) license.

1. Introduction

Al–Si alloys are widely utilized in automotive engine pistons. This is attributed to their high strength and good wear resistance [1–3]. In recent years, increasingly stringent carbon emission policies have posed greater challenges to the automotive industry. These necessitate enhancements in engine compression ratios and combustion efficiencies. Indeed, higher combustion temperatures and pressures lead to increased thermal shock to the piston, which must endure these conditions without failure. Consequently, the Al-Si alloys, as the most commonly used piston materials, must endure harsher working conditions [4].

Currently, the broadly recognized method to improve the mechanical properties of Al-Si alloys involves the addition of various alloying elements [5,6]. Certain metallic

constituents, such as Magnesium (Mg) and Copper (Cu), are solidly dissolved into the α-aluminum matrix, facilitating solid solution strengthening. Additionally, these elements are capable of precipitating as nanophases (i.e., Al-Si-Mg and Al-Si-Cu alloys) through specific heat treatment, thereby inducing a dispersion-strengthening effect [7,8]. However, the operational temperatures of these alloys are primarily determined by the thermal stability of the precipitated strengthening phases Mg_2Si and Al_2Cu, which are stable up to 185 °C and 225 °C, respectively [9,10]. Evidently, this temperature is well below the maximum operating temperature of the piston.

The integration of elements with high melting points, which do not readily amalgamate with the α-Al matrix, leads to the precipitation of intermetallic compounds of complex composition and morphology at grain boundaries through solid solution aging. This process may strengthen the grain boundaries and obstruct dislocation slip, thereby enhancing the high temperature (HT) mechanical properties of the alloy. It has been reported [11–14] that the semi-continuous network formed by intermetallic interconnections, such as ε-Al_3Ni, δ-Al_3CuNi, Q-$Al_5Cu_2Mg_8Si_6$, and γ-Al_7Cu_4Ni, plays an important role in HT mechanical properties. Asghar et al. [15,16] characterized the 3D network of the $AlSi_{12}CuMgNi$ and highlighted its importance for the mechanical properties of piston alloys. However, this 3D network structure connected by intermetallic compounds is unstable [17], which cannot be effectively improved by adjusting the alloy elements alone. Moreover, regions devoid of intermetallic compounds become fragile at HT, such as the Al-Si eutectic zone [18], especially when the engine piston is operating under the heat–mechanical loading.

Grain refinement is considered an effective method to improve the strength of alloys, in addition to adding alloying elements. Reduction in grain size amplifies the obstruction to dislocation motion and slippage, which increases the resistance to deformation and tensile strength at room temperature (RT) and HT. According to previous investigations, α-Al can be significantly refined by adding refining agents, such as Al-Ti-B and Al-Ti-C, etc., to enhance the mechanical properties in the conventional casting process [19–21]. However, the Strontium (Sr) element, commonly applied for the modification of eutectic Si, will react with the B-containing refining agent, weakening the effectiveness of both additives [22,23]. So, it is important to develop an efficient process to manufacture Al-Si alloys with a nanoscale α-Al matrix.

As a solid-state process technique, mechanical alloying (MA) is capable of fabricating nanocrystalline materials by nonequilibrium processing methods. Plenty of studies have elucidated the synthesis of nanocrystalline alloys and compounds via MA in conjunction with other heat treatment processes [24,25]. The press-forming (PF) technique is a rapid sintering method for manufacturing fully dense and nanoscale homogeneous materials [26]. Tang et al. [27] have prepared a high strength Al-Cu-Mg alloy by MA and PF, which exhibited a high tensile strength of 780 MPa and a high microhardness of 180 HV. Microstructural characterizations revealed that the grain size of α-Al was about 300 nm–5 μm. Due to its simple process and potential for manufacturing large-sized aluminum alloys, this method has attracted considerable attention and has excellent market promotion.

This study prepared a nanocrystalline Al-Si alloy with excellent thermal durability by MA and PF methods without the addition of extraneous elements. The microstructures and mechanical properties of the Al-Si alloy were investigated, and the corresponding strengthening mechanisms were discussed.

2. Experiment

2.1. Material Fabrication

The powders of Al (380 mesh, 99.7% purity) and Si (100 mesh, 99.7% purity) were used as raw materials. The as-received powders were mixed without further treatment

into Al-12Si. Mixed powders were ball milled in the vibrating high-energy ball mill (GN-2 series) (NanDa Instrument, Nanjing, Jiangsu, China) for 2 h at RT with 1470 r/min vibration frequency and with carbon steel balls (material-to-ball ratio of 12:1). To prevent oxidation and forging of the powder, acetone and ethanol were added as process control agents (PCA) for the ball milling process.

The powder mixtures were pressed at 400 MPa to the dimensions of 60 mm × 8 mm × 12 mm using a press machine (XinNuo Instrument, Shanghai, China). The cold-pressed samples were packed with graphite paper and placed in a pre-heated (at 560 °C for 3 h) mold for 3 min in 560 °C, and consequently pressed on site under 400 MPa within 30 s. After press forming, the products with dimensions of 75 mm × 6 mm × 12 mm were put out and naturally cooled to RT quickly. Schematic diagrams of the complete process are shown in Figure 1.

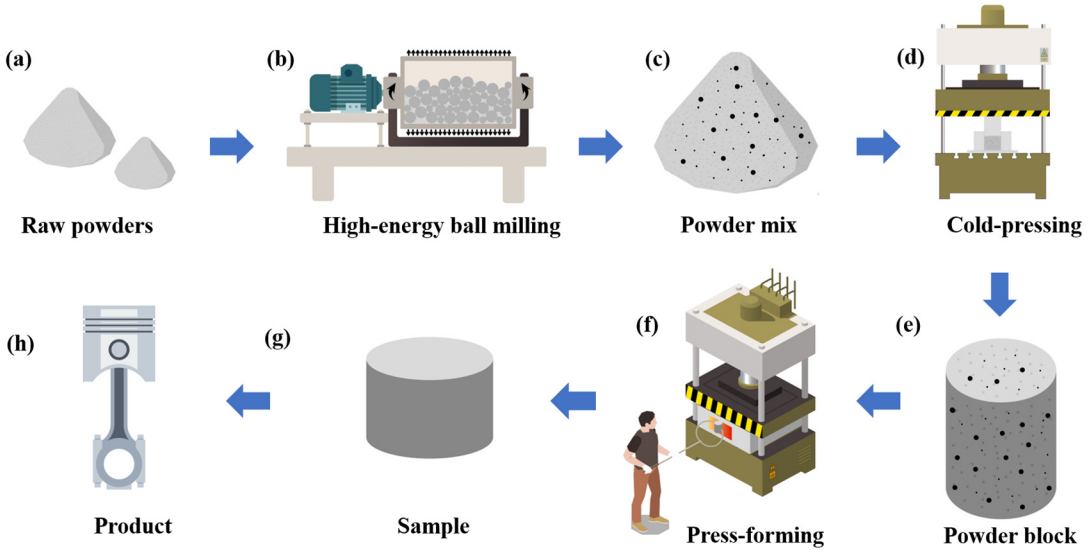


Figure 1. Schematic diagrams of the complete process. (**a**) Raw powders, (**b**) high-energy ball milling, (**c**) powder mix, (**d**) cold pressure, (**e**) powder block, (**f**) press formation, (**g**) sample, and (**h**) product.

The processing parameters used in this study were determined based on systematic preliminary optimization conducted by our research group. Different ball milling times, rotation speeds, and ball-to-powder ratios were evaluated to achieve sufficient microstructural refinement while avoiding excessive cold welding and contamination. Similarly, the press-forming temperature and pressure were optimized to ensure adequate densification without significant grain coarsening. The selected parameters were found to provide stable processing behavior and optimal mechanical performance and were therefore adopted in the present work. The optimization results are not presented here for brevity.

2.2. Microstructure Characterization and Mechanical Properties Test

The phase analysis was carried out by Bruker D8 ADVANCE X-ray diffraction (XRD) measurements (Bruker Corporation, Billerica, MA, USA) using Cu Kα radiation at 40 kV and 100 mA. Microstructures and particle morphologies were characterized by the optical microscope (OM) (Leica Microsystems GmbH, Wetzlar, Germany) and field emission scanning electron microscopy (FESEM, TESCAN CLARA GMH). The distribution patterns of Al and Si phases were characterized by high-resolution transmission electron microscopes (HRTEM, FEI Talos F200X) (FEI Company, Hillsboro, OR, USA).

The samples were placed in a chamber resistance furnace (SXL-1200C) (Jvjing Precision Instrument, Shanghai, China) for heat exposure experiments. The samples were held at 200 °C, 350 °C, and 400 °C for 25 h, 50 h, 100 h, 200 h, 500 h, and 1000 h, respectively, to

investigate the effects of heat exposure temperature and time on the microstructure and mechanical properties of the alloy. In the following, the Al-12Si alloys prepared by MA and PF are labeled as Alloy A. Alloy A samples after heat exposure at 200 °C, 350 °C, and 400 °C are labeled as Alloy-200 °C, Alloy-350 °C, and Alloy-400 °C, respectively.

The temperatures for isothermal heat exposure ("annealing") and high-temperature tensile testing were selected to bracket representative thermal service conditions of Al-Si piston alloys and to correlate with the thermal stability of the strengthening microstructure. In practical engine applications, the typical working temperatures of modern Al-Si piston alloys can reach 250–350 °C, where strength retention becomes critical; therefore, 350 °C was chosen as the primary target temperature for both long-term exposure and tensile testing [28]. A temperature of 200 °C was selected as a lower-bound temperature representing moderate thermal loading relevant to powertrain alloys, providing a baseline condition in which microstructural degradation is less pronounced compared with higher service temperatures [29]. A temperature of 400 °C was chosen as an over-temperature/accelerated condition, consistent with the literature that sets upper exposure temperatures up to 400 °C to simulate the thermal conditions of different piston regions and to probe accelerated microstructural evolution [30]. Using the same temperature set for exposure and tensile testing enables a direct linkage between microstructural evolution and the corresponding strength degradation.

Tensile testing: Room-temperature tensile specimens were machined into a flat dog-bone geometry with the following dimensions: grip width 8 mm, grip length 10 mm, gauge width 3 mm, gauge length 15 mm, and filet radius R4. The specimen thickness was measured for each specimen prior to testing. The initial cross-sectional area of the gauge section was calculated from the measured gauge width and thickness.

Elevated-temperature tensile specimens were flat pin-loaded specimens with an overall length of 70 mm. Each end tab was 14 mm in length and 10 mm in width, with a pin-hole diameter of Φ4 mm. The gauge section width was 5 mm, and the gauge thickness was 3 mm. The end-tab thickness was 5 mm, and the transition between the gauge section and end tabs had a filet radius of R2. Elevated-temperature tensile tests were conducted at 200 °C, 350 °C, and 400 °C, with a crosshead speed of 1 mm/min.

Prior to elevated-temperature tensile testing, the specimens were held (soaked) at the target temperature for 30 min to ensure thermal equilibrium and to minimize temperature gradients across the gauge section. This pre-hold improves the repeatability and comparability of high-temperature tensile data by stabilizing the specimen's temperature before loading.

For each condition, at least three specimens were tested to minimize experimental scatter.

In this study, mechanical property evaluation is focused on tensile behavior and its long-term stability under thermal exposure, which are most relevant to the targeted application; compression testing is beyond the scope of the present work.

3. Results and Discussion

3.1. Powder Characterization

Figure 2a,b display the SEM morphological images of raw Al and Si powders. It is evident that the Al powders are spherical in shape, exhibiting a uniform particle size distribution. In contrast, the Si powder consists of sharp polyhedrons. Following extensive violent impact via the MA method, the shapes of the Al-12Si mixed powders appear irregular, as shown in Figure 2c, predominantly exhibiting flat flakes with few particles resembling spherical shapes. Notably, there is a wide range of particle size distributions in the mixed powders, which is distinctly different from that of the Al and Si powders. Figure 2d also presents a typical XRD pattern of Al and Si powders, as well as Al-12Si

powders after MA. Compared to the curves of raw Al and Si powders, the diffraction peak intensity of the Al-Si mixed powder after ball milling broadens, primarily due to grain refinement and lattice distortion induced by MA during the ball milling process. Figure 2d presents the XRD patterns of the mixed Al-Si powders after mechanical alloying. Only diffraction peaks corresponding to Al and Si phases are observed. No additional crystalline oxide (e.g., Al_2O_3) or carbide (e.g., Al_4C_3) phases are detected within the detection limit of XRD. It should be noted that XRD is not sensitive to amorphous oxide layers or trace interstitial concentrations; therefore, the presence of a small amount of non-crystalline oxygen or carbon cannot be completely excluded. Acetone and ethanol were used as process control agents (PCAs) during milling to suppress excessive cold welding. Considering the relatively short milling duration (2 h), severe PCA decomposition is unlikely, and no crystalline by-products associated with PCA decomposition were identified in the XRD results.

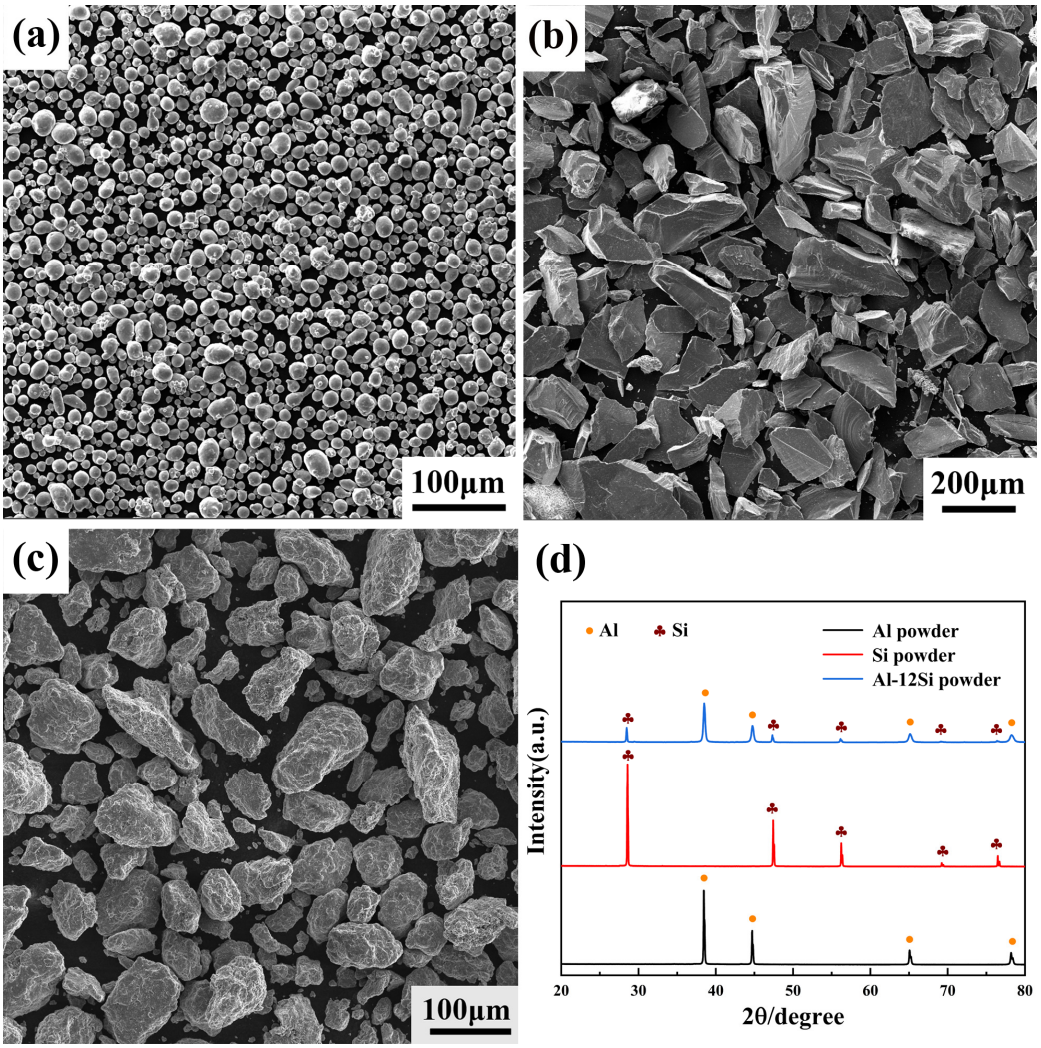


Figure 2. SEM images and particle size distributions of different powders: (**a**) Al powder, (**b**) Si powder, and (**c**) Al-12Si powder after MA. (**d**) Typical XRD patterns of the Al, Si powder, and Al-Si powder after MA.

3.2. Mechanical Properties

Figure 3a,b illustrate the variations in ultimate tensile strength (UTS) and the elongation of Alloy A, Alloy-200 °C, Alloy-350 °C, and Alloy-400 °C for different heat exposure durations at RT, respectively. As depicted in Figure 3a, the UTS of Alloy A is 457 MPa with 0.5% elongation, which is significantly higher than the 195 MPa of conventional casting

Al-12Si alloys [31]. About a 10% drop was observed after 200 h of heat exposure for all three elevated temperatures. Notably, at 200 °C and 350 °C, Al-12Si could still maintain its performance after 1000 h of treatment, while at 400 °C, the performance drop was significant. A similar temperature-accelerated degradation as the exposure temperature approaches ~400 °C has been reported for Al-Si piston alloys, which is commonly linked to accelerated microstructural evolution during thermal exposure [30]. Additionally, as shown in Figure 3b, the elongation of Alloy-200 °C remains relatively stable during heat exposure and reaches approximately 0.62% after 1000 h. In contrast, the elongation of Alloy-350 °C increases gradually with heat exposure time, reaching about 0.75% after 1000 h. A more pronounced increase is observed for Alloy-400 °C, where the elongation rises to approximately 1.12% after 1000 h. The hardness of the alloys exhibits a normal decreasing trend with the rise in the heat exposure temperature and the extension of heat exposure time, as shown in Figure 3c. Upon careful observation, after 25 h of heat exposure, the hardness of the alloys decreased rapidly and then slowed down. After 1000 h, the hardness ultimately decreased by 82 HB, 96 HB, and 122 HB, respectively. It is evident that the Al-12Si alloys prepared by the MA + PF method demonstrate excellent mechanical properties at RT, which surprisingly remain effective even after long-term heat exposure (1000 h) at 350 °C, matching the actual working temperature of the piston [26].

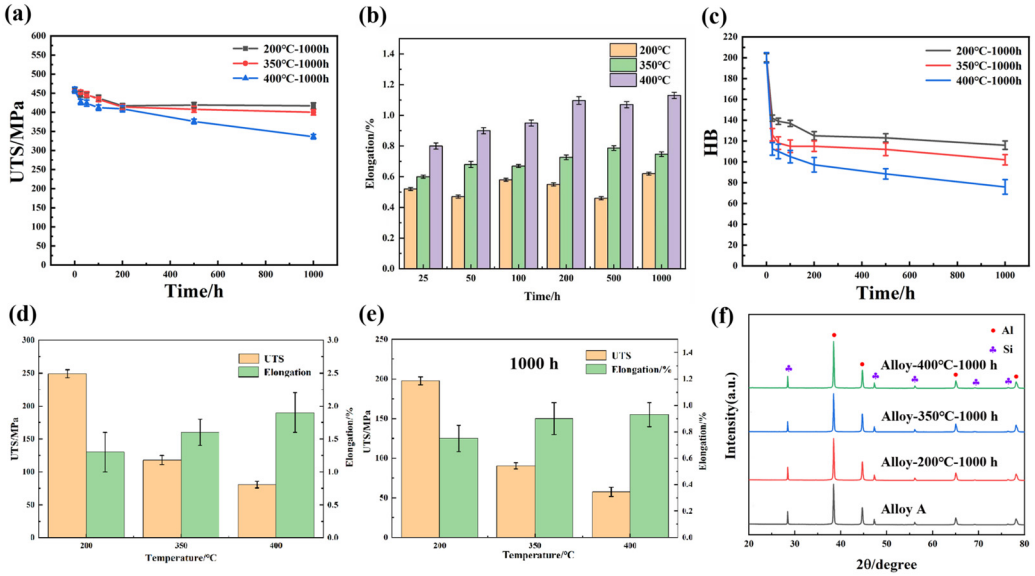


Figure 3. (**a**–**c**) represent the ultimate tensile strength (UTS), elongation, and hardness of Alloy A, Alloy-200 °C, Alloy-350 °C, and Alloy-400 °C with different heat exposure times at room temperature (RT), respectively; (**d**,**e**) show the UTS and elongation of Alloy A, Alloy-200 °C (0 h and 1000 h), Alloy-350 °C (0 h and 1000 h), and Alloy-400 °C (0 h and 1000 h) tested at high temperatures (HTs); and (**f**) shows the typical XRD patterns of Alloy A, Alloy-200 °C-1000 h, Alloy-350 °C-1000 h, and Alloy-400 °C-1000 h.

To investigate the HT mechanical properties of alloys, the UTS and elongation of Alloy A, Alloy-200 °C-(0 h and 1000 h), Alloy-350 °C-(0 h and 1000 h), and Alloy-400 °C-(0 h and 1000 h) at HTs have been measured, with the results illustrated in Figure 3d,e. As depicted in Figure 3d, the UTS of the alloy without heat exposure treatment shows an excellent value (250 MPa) at 200 °C. It is noteworthy that the UTS of the alloy is significantly higher than that reported in other studies (Table 1) at 350 °C (the working temperature of the piston), demonstrating advantages achieved solely through MA + PF methods without any adjustment of alloy components. For comparison, composition-designed piston alloys (e.g., Al-Si-Cu-Ni-Mg systems) typically achieve lower UTS levels at 350 °C under comparable testing conditions. Therefore, the 350 °C UTS of 118 MPa obtained

here indicates a competitive high-temperature strength level relative to representative heat-resistant piston alloys reported in the literature [1]. When the testing temperature rises to 400 °C, the UTS of the alloy can remain at 80 MPa. Overall, whether at RT or under various HTs testing conditions, the UTSs of the Al-12Si alloys using the MA + PF methods were exceptionally impressive, far surpassing traditional casting alloys with composition adjustments [31].

Table 1. The UTSs of Al-Si alloys at 350 °C.

Materials Composition (wt. %)	UTS (MPa)	Ref.
Al-12Si (MA + PF)	**118**	**This work**
Al-12Si-3.5Cu-2Mn-1Cr	106	[32]
Al-12Si-4Cu-2Ni-1Mg-AlNp	106	[1]
Al-12Si-3Cu-1.5Ni	62	[33]
Al-12Si-3.5Cu-0.2Fe-2Mn	83	[32]
Al-12Si-3Cu-2Ni-1Mg	65	[34]

Bold entries indicate the results obtained in this work.

For automotive engine pistons, the long-term HT stability of alloy materials is a crucial performance indicator. Therefore, after 1000 h of various temperature heat exposure tests, the HT-UTS of the alloys (Alloy-200 °C-1000 h, Alloy-350 °C-1000 h, and Alloy-400 °C-1000 h) were also tested, as shown in Figure 3e. The UTS of Alloy-200 °C decreased from 250 MPa to 198 MPa as the heat exposure time increased from 0 h to 1000 h. When the heat exposure temperature rises to 350 °C and 400 °C for 1000 h, the HT-UTS of Alloy-350 °C and Alloy-400 °C are 90 MPa and 58 MPa, respectively. It is evident that after 1000 h of heat exposure at 200 °C and 350 °C, the HT-UTS of the alloys decreased slightly by 20% and 23%, respectively, compared to the more significant decrease of 35% observed at 400 °C for 1000 h. In addition, it can be observed that the increase in heat exposure temperature and the extension of the heat exposure time may contribute to the growth of the grain size, which results in increased elongation. To characterize the microscopic phase changes in alloys exposed to different temperatures for an extended period, the typical XRD pattern curves of Alloy A, Alloy-200 °C, Alloy-350 °C, and Alloy-400 °C for 1000 h are presented in Figure 3f. As the temperature increased, the diffraction peak intensities of Al and Si continuously rose, while the diffraction peak widths narrowed, which is characteristic of grain growth. Moreover, there are no other diffraction peaks present except for Al and Si. To further illustrate the deformation behavior beyond the summarized UTS and elongation values in Figure 3, the full engineering stress–strain curves are presented in Figure 4.

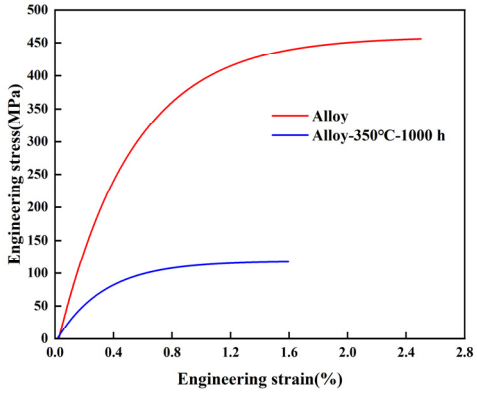


Figure 4. Engineering stress–strain curves of the alloy at room temperature (as prepared) and after thermal exposure at 350 °C for 1000 h (crosshead speed: 1 mm/min).

Figure 4 compares the engineering stress–strain curves of the alloy at room temperature in the as-prepared condition and after thermal exposure at 350 °C for 1000 h. The as-prepared alloy exhibits a high UTS of 458 MPa with an elongation of 2.5%, indicating a high-strength but limited-ductility response. After 350 °C/1000 h exposure, the flow stress decreases substantially, and the curve shows reduced strain-hardening capability, resulting in a lower UTS of 118 MPa and an elongation of 1.6%. This pronounced reduction in both strength and ductility is consistent with thermally induced microstructural evolution during long-term exposure and supports the strength-retention trend summarized in Figure 3.

3.3. Microstructure Analysis

Figure 5a presents the optical microstructure image of Alloy A, which exhibited a tensile strength of 458 MPa at RT. The Si particles are primarily bulk-like with a uniform distribution, and their size is less than 5 μm, contributing significantly to dispersion strengthening. Notably, the silicon particles in the alloy produced by the MA + PF method differ from the pentagonal twin Si particles [35], which require morphological control in casting [36], and which can effectively reduce stress concentration and enhance the mechanical properties of the material. To analyze the variations in size and morphology of silicon particles at different heat exposure temperatures, the OM morphological images of Alloy A, Alloy-200 °C-1000 h, Alloy-350 °C-1000 h, and Alloy-400 °C-1000 h were obtained and are presented in Figure 5b–d. Correspondingly, the equivalent diameter and shape factor of the silicon particles were also generated and displayed in Figure 5e. It is evident that the size of the silicon particles gradually increased with rising heat exposure temperatures, leading to a reduction in the dispersion strengthening effect. More importantly, the shape factor decreased from 0.9 to 0.73 as the heat exposure temperature increased, indicating a reduction in the spheroidization degree of the Si phase. Consequently, the alloy became more susceptible to cracking at the sharp corners of the Si phase, resulting in diminished mechanical properties. This interpretation is consistent with prior observations that the cracking/debonding of brittle Si particles is a dominant crack initiation mechanism in cast Al-Si alloy [18].

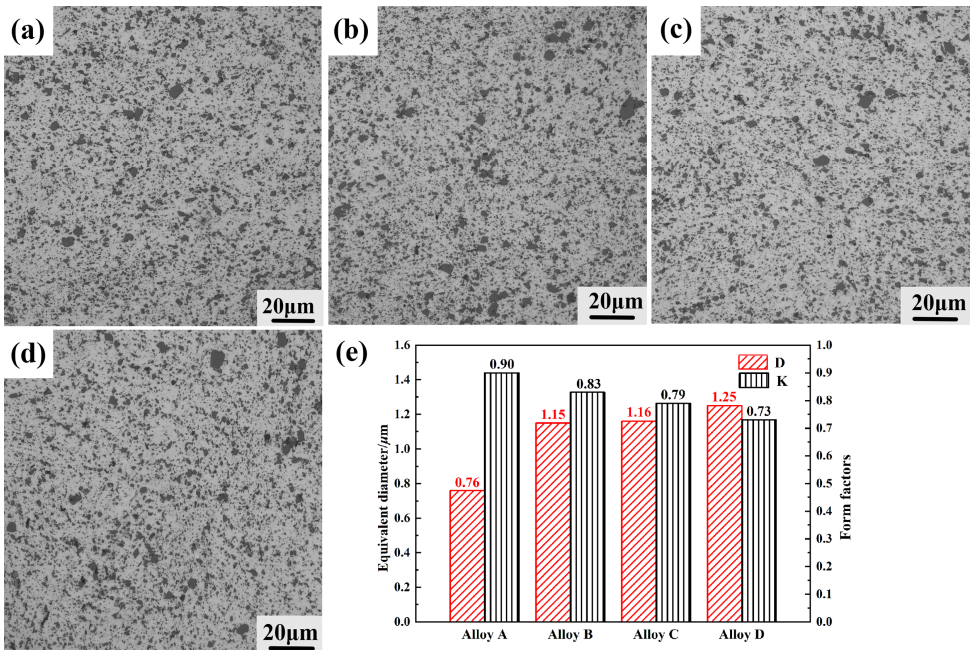


Figure 5. (**a**–**d**) OM morphological images of Alloy A, Alloy-200 °C-1000 h, Alloy-350 °C-1000 h, and Alloy-400 °C-1000 h; (**e**) the equivalent diameter and shape factor of silicon particles in (**a**–**d**).

TEM observation has been conducted to characterize the strengthening mechanism of the Al-12Si alloys through MA + PF. As illustrated in Figure 6a, the grain morphology of the Al matrix exhibits a homogeneous distribution with a small average size of approximately 300 nm, which contributes to the strengthening effect of fine grains. As the grain sizes decrease, the total area of grain boundaries per unit volume increases, providing more obstacles for dislocation motion and enhancing the strength of the alloys. Moreover, the accumulation of dislocations at grain boundaries generates stress fields that can activate additional dislocation sources in neighboring grains, increasing the strength in the polycrystalline Al matrix. The finer the grain size, the more grain boundaries are involved in the slip, which aids in improving the plasticity of the alloys and reducing the likelihood of local stress concentration. Notably, high-density stacking fault (SF) structures were observed in the Al matrix, as shown in Figure 6b, with high stacking fault formation energy [37,38]. The presence of SFs increases the defect energy of the alloys, enhancing their resistance to deformation and requiring a higher energy barrier for plastic deformation. SFs act as obstacles to dislocation movement, necessitating that dislocations either circumvent or cut through these faults by expending additional energy, thereby increasing the strength of the alloys. In this work, the raw materials consist of pure Al powders and pure Si powders, with no other alloying elements artificially added.

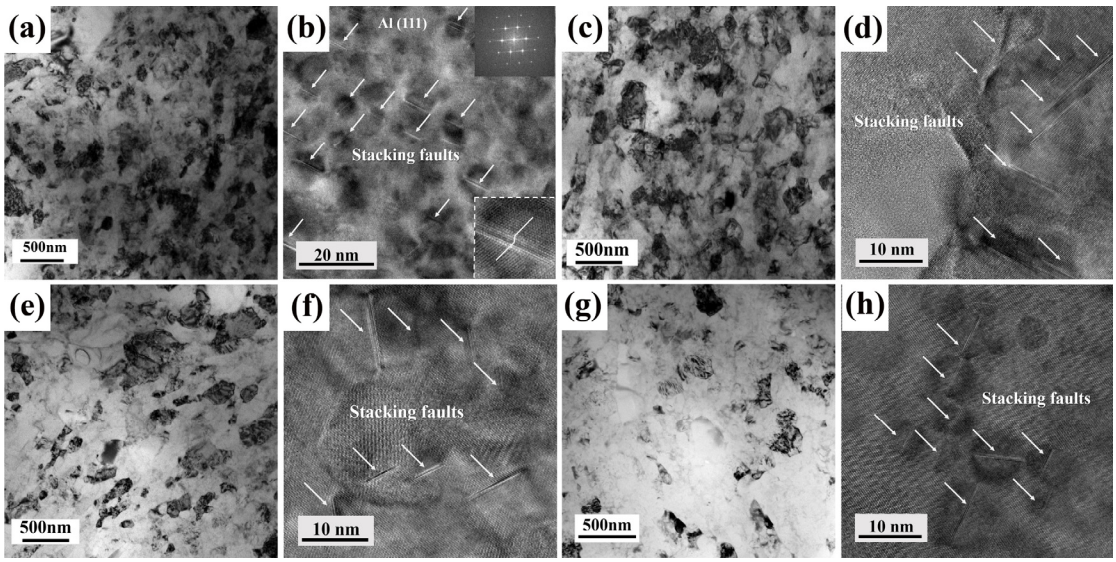


Figure 6. (**a**,**c**,**e**,**g**) present TEM bright field images of Alloy A, Alloy-200 °C-1000 h, Alloy-350 °C-1000 h, and Alloy-400 °C-1000 h concerning the Al-matrix, respectively; (**b**,**d**,**f**,**h**) display HRTEM images of Alloy A, Alloy-200 °C-1000 h, Alloy-350 °C-1000 h, and Alloy-400 °C-1000 h regarding the Al-matrix, respectively.

It is evident that the combination of fine-grain strengthening and stacking fault strengthening serves as the primary mechanism for the excellent RT mechanical properties of Al-Si prepared using MA + PF methods. Compared with cast piston alloys that obtain elevated-temperature strength mainly from rigid multiphase/intermetallic networks, the present alloy achieves competitive thermal stability through MA + PF-enabled microstructural refinement and defect stabilization [15].

Compared to Figure 6a,c,e,g, the grain sizes in the Al-matrix increase only slightly with the rise in heat exposure temperature, according to statistics. A gradual reduction in the number of visible stacking faults can be observed in Figure 6b to Figure 6h. To provide a semi-quantitative comparison, the number of visible stacking faults within comparable HRTEM observation areas was estimated for each condition. In Alloy A (Figure 6b), approximately 14–16 stacking faults can be identified within a representative region. After

heat exposure at 200 °C for 1000 h (Figure 6d), the number decreases to about 9–10 faults. A further reduction is observed in Alloy-350 °C-1000 h (Figure 6f), where only 6–7 faults are visible. For Alloy-400 °C-1000 h (Figure 6h), the number of stacking faults decreases to approximately 4–5 within similar observation areas. This trend is consistent with the observed decrease in tensile strength.

To understand the failure mechanism of the alloys at elevated temperatures, the tensile fracture surfaces of the specimens were characterized using SEM. From the fracture morphology at different magnifications in Figure 7a–c, the larger Si particles in Alloy A generate secondary cracks during plastic deformation due to stress concentration, which primarily occurs within the grains. During the stretching process, Si particles experience significant cleavage fracture, resulting in numerous smooth and flat cleavage surfaces. At the interface between Si particles and the Al matrix, a considerable number of tearing ridges are observed. Overall, the fracture mode of Alloy A under RT tensile conditions is brittle transgranular fracture.

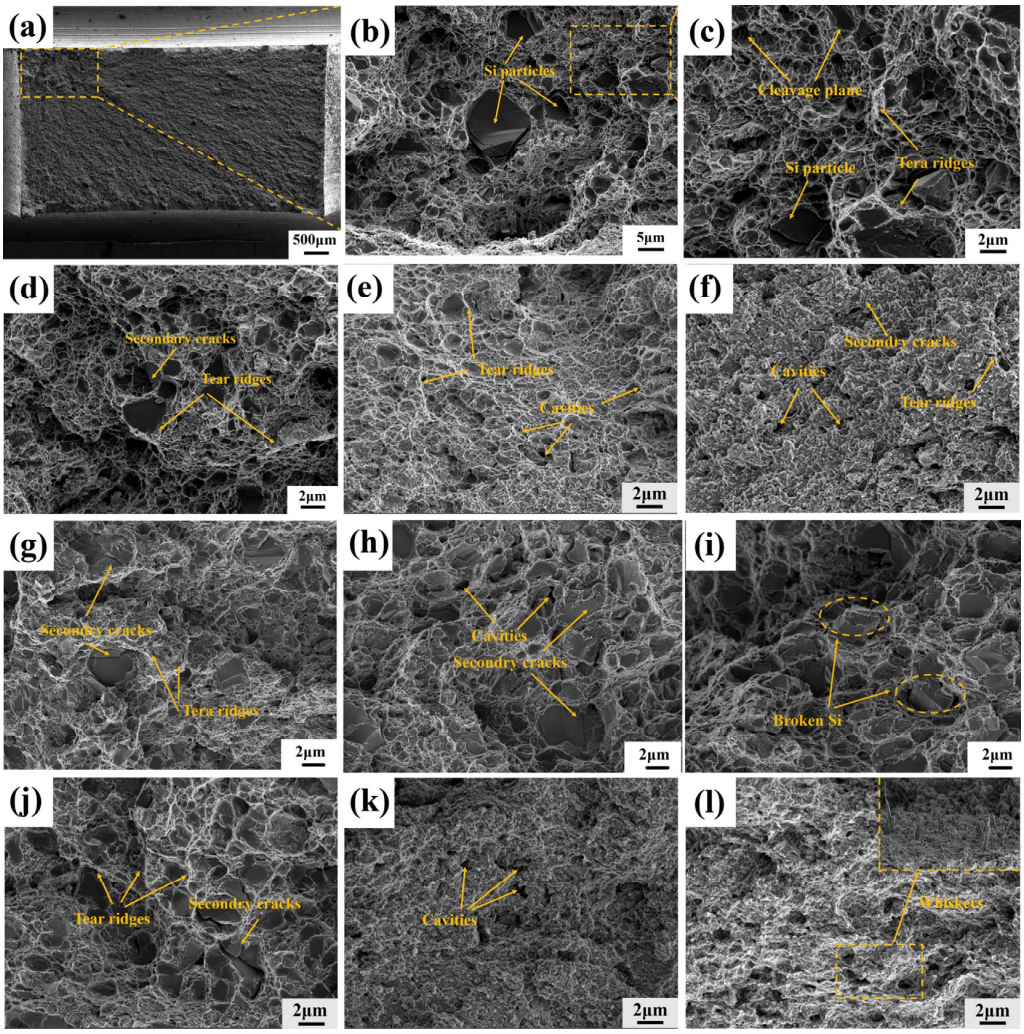


Figure 7. Fractographs of tensile specimens: (**a**–**c**) show different magnifications of Alloy A at room temperature (RT); (**d**–**f**) show Alloy A tested at 200 °C, 350 °C, and 400 °C, respectively; (**g**–**i**) correspond to Alloy-200 °C-1000 h, Alloy-350 °C-1000 h, and Alloy-400 °C-1000 h tested at RT; and (**j**–**l**) show the high-temperature tensile fracture morphologies of Alloy-200 °C-1000 h, Alloy-350 °C-1000 h, and Alloy-400 °C-1000 h, respectively.

Figure 7d–f illustrate the fracture morphology of Alloy A at 200 °C, 350 °C, and 400 °C, respectively. At varying temperatures, secondary cracks are evident in Si particles, and

numerous cavities resulting from Si particle debonding are present on the fracture surface. At 200 °C, as shown in Figure 7d, a significant number of fractured Si particles can be seen on the fracture surface, which displays typical brittle quasi-cleavage characteristics. As the temperature increases, tearing ridges emerge around Si particles or defects, and cleavage steps become noticeable during HT at 400 °C. Similar to other aluminum-based reinforced composite materials, this alloy, produced by MA + PF, exhibits brittle fracture at the macroscopic level and ductile fracture at the microscopic level [39].

Figure 7a–c show the RT tensile fracture morphology of Alloy A at different magnifications, while Figure 7g–i correspond to the RT fracture morphologies of Alloy-200 °C-1000 h, Alloy-350 °C-1000 h, and Alloy-400 °C-1000 h, respectively.

Obviously, as the heat exposure temperature increases, there is no significant alteration in the RT fracture morphology of the alloys. Among them, Si particles are uniformly distributed within the Al-matrix, with sizes ranging from approximately 2–10 μm. The fracture surface exhibits typical intergranular fracture, which suggests that larger Si particles, tear ridges, and defects are the main triggers of crack initiation.

Figure 7j–l illustrate the HT tensile fracture morphology of Alloy-200 °C-1000 h, Alloy-350 °C-1000 h, and Alloy-400 °C-1000 h after heat exposure. Similar to the HT tensile fracture of Alloy A, the fracture still displays intergranular characteristics at 250 °C. As the heat exposure and measurement temperature increase, cavities formed by the extraction of Si particles and whiskers become visible on the fracture surface, while the extracted whiskers can be observed on the opposite side of the fracture depicted in Figure 7l. It is evident that the Si phase is susceptible to stress concentration and microcracks at this temperature due to the significant difference in the elastic modulus between the Si phase and Al-matrix [40,41].

4. Conclusions

In the present work, a high-strength Al-12Si alloy was prepared via the MA and PF processes without any adjustment of the alloy components. The microstructures and mechanical properties were investigated, leading to the following conclusions:

(1) The alloy exhibited excellent mechanical properties at both RT (UTS 457 MPa) and HT (UTS 118 MPa at 350 °C).
(2) The alloy also demonstrated remarkable long-term HT stability after heat exposure for 1000 h, with XRD characterizations confirming that it consists solely of an Al matrix and Si phase.
(3) TEM analysis revealed that the grain size of the Al matrix was approximately 300 nm, and there were high-density stacking faults in the Al matrix. The strengthening mechanisms involved in the Al-12Si alloys can primarily be attributed to grain refinement strengthening and stacking fault strengthening.

According to the Hall–Petch relationship, the yield strength can be expressed as:

$$\sigma_y = \sigma_0 + kd^{-1/2}$$

where σ_y is the yield strength (MPa), σ_0 is the friction stress (MPa), k is the Hall–Petch coefficient (MPa·m$^{1/2}$), and d is the average grain size (m). For Al alloys, k typically ranges from 0.07 to 0.15 MPa·m$^{1/2}$. Considering the ultrafine grain size (~300 nm) achieved in the present alloy, grain boundary strengthening contributes significantly to the overall strength compared with conventional cast Al-Si alloys with micrometer-scale grains. Therefore, grain refinement introduced by the MA + PF process is one of the primary strengthening mechanisms.

In addition to grain boundary strengthening, high-density stacking faults generated during mechanical alloying further impede the dislocation motion. Stacking faults act as planar defects that subdivide grains and introduce local lattice distortion, thereby increasing the resistance to dislocation glide. The semi-quantitative reduction in visible stacking faults after heat exposure correlates with the decrease in tensile strength, indicating that stacking fault strengthening contributes significantly to the superior mechanical performance of the as-processed alloy.

Compared with previously reported nanocrystalline Al alloys prepared by severe plastic deformation or mechanical alloying, where rapid grain coarsening and defect recovery often occur at elevated temperatures, the present alloy maintains a substantial fraction of ultrafine grains and stacking faults even after 1000 h of heat exposure. This suggests the improved thermal stability of the defect structure, which is beneficial for high-temperature applications such as piston components operating at ~350 °C. Compared with representative composition-designed heat-resistant Al-Si piston alloys reported in the literature, the present alloy exhibits competitive tensile strength at 350 °C (118 MPa) without extraneous alloying additions.

Author Contributions: Conceptualization, H.T., L.S., W.Z. and Z.Y.; methodology, H.T. and W.Z.; software, L.Z., X.W., P.J. and Y.Z.; validation, L.Z., C.X., J.L., J.Z. (Junchen Zhang), J.Z. (Junfeng Zhang) and X.W.; formal analysis, J.L., J.Z. (Junchen Zhang) and J.Z. (Junfeng Zhang); investigation, L.Z., L.S. and C.X.; resources, H.T.; data curation, L.Z., L.S. and C.X.; writing—original draft preparation, L.Z., L.S., C.X. and Z.R.; writing—review and editing, H.T., W.Z. and L.S.; visualization, L.S., Y.Z. and P.J.; supervision, H.T., W.Z. and Z.Y.; project administration, H.T., W.Z. and L.S.; funding acquisition, H.T. All authors have read and agreed to the published version of the manuscript.

Funding: This work was supported by the Shandong Provincial Natural Science Foundation (ZR2020ZD29, ZR2021JQ20, ZR2023QE317, ZR2023QE065), the program of Shandong Laboratory (SYS202204), the Key R&D Program of Shandong Province, China (2024CXGC010316) and the Taishan Scholars Program of Shandong Province and the Taishan Industrial Experts Program of Shandong Province.

Data Availability Statement: The raw data supporting the conclusions of this article will be made available by the authors on request. The raw/processed data required to reproduce these findings cannot be shared at this time as the data also forms part of an ongoing study.

Conflicts of Interest: Author Huaguo Tang was employed by the company Yantai Huihua Metal Sci. & Tech. Authors Jingtao Liu, Junchen Zhang and Junfeng Zhang were employed by the company Shandong Ludian Line Equipment. The remaining authors declare that the research was conducted in the absence of any commercial or financial relationships that could be construed as a potential conflict of interest.

References

1. Hu, K.; Xu, Q.; Ma, X.; Sun, Q.; Gao, T.; Liu, X. A novel heat-resistant Al–Si–Cu–Ni–Mg base material synergistically strengthened by Ni-rich intermetallics and nano-AlNp microskeletons. *J. Mater. Sci. Technol.* **2019**, *35*, 306–312. [CrossRef]
2. Li, J.; Albu, M.; Hofer, F.; Schumacher, P. Solute adsorption and entrapment during eutectic Si growth in A–Si-based alloys. *Acta Mater.* **2015**, *83*, 187–202. [CrossRef]
3. Yuan, Z.; Guo, Z.; Xiong, S. Effect of as-cast microstructure heterogeneity on aging behavior of a high-pressure die-cast A380 alloy. *Mater. Charact.* **2018**, *135*, 278–286. [CrossRef]
4. Zuo, L.; Ye, B.; Feng, J.; Kong, X.; Jiang, H.; Ding, W. Microstructure, tensile properties and creep behavior of Al-12Si-3.5 Cu-2Ni-0.8 Mg alloy produced by different casting technologies. *J. Mater. Sci. Technol.* **2018**, *34*, 1222–1228. [CrossRef]
5. Bobel, A.; Kim, K.; Wolverton, C.; Walker, M.; Olson, G.B. Equilibrium composition variation of Q-phase precipitates in aluminum alloys. *Acta Mater.* **2017**, *138*, 150–160. [CrossRef]
6. Jung, J.-G.; Lee, J.-M.; Cho, Y.-H.; Yoon, W.-H. Combined effects of ultrasonic melt treatment, Si addition and solution treatment on the microstructure and tensile properties of multicomponent AlSi alloys. *J. Alloys Compd.* **2017**, *693*, 201–210. [CrossRef]

7. Farkoosh, A.; Pekguleryuz, M. Enhanced mechanical properties of an Al–Si–Cu–Mg alloy at 300 C: Effects of Mg and the Q-precipitate phase. *Mater. Sci. Eng. A* **2015**, *621*, 277–286. [CrossRef]
8. Cheng, W.; Liu, C.; Huang, H.; Zhang, L.; Zhang, B.; Shi, L. High strength and ductility of Al–Si–Mg alloys fabricated by deformation and heat treatment. *Mater. Charact.* **2021**, *178*, 111278. [CrossRef]
9. Abdulwahab, M.; Madugu, I.; Yaro, S.; Hassan, S.B.; Popoola, A. Effects of multiple-step thermal ageing treatment on the hardness characteristics of A356. 0-type Al–Si–Mg alloy. *Mater. Des.* **2011**, *32*, 1159–1166. [CrossRef]
10. Toda, H.; Nishimura, T.; Uesugi, K.; Suzuki, Y.; Kobayashi, M. Influence of high-temperature solution treatments on mechanical properties of an Al–Si–Cu aluminum alloy. *Acta Mater.* **2010**, *58*, 2014–2025. [CrossRef]
11. Manasijevic, S.; Radisa, R.; Markovic, S.; Acimovic-Pavlovic, Z.; Raic, K. Thermal analysis and microscopic characterization of the piston alloy AlSi13Cu4Ni2Mg. *Intermetallics* **2011**, *19*, 486–492. [CrossRef]
12. Sun, Y.; Li, C.; Liu, Y.; Yu, L.; Li, H. Intermetallic phase evolution and strengthening effect in Al–Mg2Si alloys with different Cu/Ni ratios. *Mater. Lett.* **2018**, *215*, 254–258. [CrossRef]
13. Li, Y.; Yang, Y.; Wu, Y.; Wei, Z.; Liu, X. Supportive strengthening role of Cr-rich phase on Al–Si multicomponent piston alloy at elevated temperature. *Mater. Sci. Eng. A* **2011**, *528*, 4427–4430. [CrossRef]
14. Li, Y.; Yang, Y.; Wu, Y.; Wang, L.; Liu, X. Quantitative comparison of three Ni-containing phases to the elevated-temperature properties of Al–Si piston alloys. *Mater. Sci. Eng. A* **2010**, *527*, 7132–7137. [CrossRef]
15. Asghar, Z.; Requena, G.; Boller, E. Three-dimensional rigid multiphase networks providing high-temperature strength to cast AlSi10Cu5Ni1-2 piston alloys. *Acta Mater.* **2011**, *59*, 6420–6432. [CrossRef]
16. Asghar, Z.; Requena, G.; Degischer, H.; Cloetens, P. Three-dimensional study of Ni aluminides in an AlSi12 alloy by means of light optical and synchrotron microtomography. *Acta Mater.* **2009**, *57*, 4125–4132. [CrossRef]
17. Dezecot, S.; Buffiere, J.-Y.; Koster, A.; Maurel, V.; Szmytka, F.; Charkaluk, E.; Dahdah, N.; El Bartali, A.; Limodin, N.; Witz, J.-F. In situ 3D characterization of high temperature fatigue damage mechanisms in a cast aluminum alloy using synchrotron X-ray tomography. *Scr. Mater.* **2016**, *113*, 254–258. [CrossRef]
18. Gall, K.; Yang, N.; Horstemeyer, M.; McDowell, D.L.; Fan, J. The debonding and fracture of Si particles during the fatigue of a cast Al-Si alloy. *Metall. Mater. Trans. A* **1999**, *30*, 3079–3088. [CrossRef]
19. Zhang, L.; Zheng, Q.; Jiang, H.; Zhao, J. Interfacial energy between Al melt and TiB2 particles and efficiency of TiB2 particles to nucleate α-Al. *Scr. Mater.* **2019**, *160*, 25–28. [CrossRef]
20. Fan, Z.; Wang, Y.; Zhang, Y.; Qin, T.; Zhou, X.; Thompson, G.; Pennycook, T.; Hashimoto, T. Grain refining mechanism in the Al/Al–Ti–B system. *Acta Mater.* **2015**, *84*, 292–304. [CrossRef]
21. Tan, P.; Yang, Y.; Sui, Y.; Wang, Q.; Jiang, Y. The influence of Al–10Sr or/and Al–5Ti–1B on microstructure and mechanical properties of Al–12Si–4Cu–2Ni–0.8 Mg alloys. *J. Alloys Compd.* **2019**, *809*, 151856. [CrossRef]
22. Liao, H.; Sun, G. Mutual poisoning effect between Sr and B in Al–Si casting alloys. *Scr. Mater.* **2003**, *48*, 1035–1039. [CrossRef]
23. Birol, Y. Melt treatment of Al–Si foundry alloys with B and Sr additions. *J. Mater. Sci.* **2017**, *52*, 6856–6865. [CrossRef]
24. Deaquino-Lara, R.; Gutiérrez-Castañeda, E.; Estrada-Guel, I.; Hinojosa-Ruiz, G.; García-Sánchez, E.; Herrera-Ramírez, J.; Pérez-Bustamante, R.; Martínez-Sánchez, R. Structural characterization of aluminium alloy 7075–graphite composites fabricated by mechanical alloying and hot extrusion. *Mater. Des.* **2014**, *53*, 1104–1111. [CrossRef]
25. Soltani, N.; Nodooshan, H.J.; Bahrami, A.; Pech-Canul, M.; Liu, W.; Wu, G. Effect of hot extrusion on wear properties of Al–15 wt.% Mg2Si in situ metal matrix composites. *Mater. Des.* **2014**, *53*, 774–781. [CrossRef]
26. Liu, T.; Li, A.; Zhu, C.; Yuan, W. Effect of alloying elements on surface temperature field of aluminum piston in diesel engine. *Eng. Fail. Anal.* **2022**, *134*, 106020. [CrossRef]
27. Tang, H.; Cheng, Z.; Liu, J.; Ma, X. Preparation of a high strength Al–Cu–Mg alloy by mechanical alloying and press-forming. *Mater. Sci. Eng. A* **2012**, *550*, 51–54. [CrossRef]
28. Jin, L.; Liu, K.; Chen, X.-G. Improved elevated temperature properties in Al-13%Si piston alloys by Mo addition. *J. Mater. Eng. Perform.* **2020**, *29*, 126–134. [CrossRef]
29. Shaha, S.K.; Czerwinski, F.; Kasprzak, W.; Friedman, J.; Chen, D.L. Ageing characteristics and high-temperature tensile properties of Al–Si–Cu–Mg alloys with micro-additions of Cr, Ti, V and Zr. *Mater. Sci. Eng. A* **2016**, *652*, 353–364. [CrossRef]
30. An, H.; Geng, J.; Bian, Z.; Liu, G.; Wang, M.; Chen, D.; Wang, H. Morphological Evolutions of Ni-Rich Phases in Al-Si Piston Alloys during 250–400 °C Thermal Exposure Processes. *Materials* **2020**, *13*, 5212. [CrossRef]
31. Warmuzek, M. *Aluminum-Silicon Casting Alloys*; ASM International: Almere, The Netherlands, 2004; pp. 1–6.
32. Li, G.; Liao, H.; Suo, X.; Tang, Y.; Dixit, U.S.; Petrov, P. Cr-induced morphology change of primary Mn-rich phase in Al-Si-Cu-Mn heat resistant aluminum alloys and its contribution to high temperature strength. *Mater. Sci. Eng. A* **2018**, *709*, 90–96. [CrossRef]
33. Zuo, L.; Ye, B.; Feng, J.; Xu, X.; Kong, X.; Jiang, H. Effect of δ-Al3CuNi phase and heat exposure on microstructure and mechanical properties of Al-Si-Cu-Ni alloys. *J. Alloys Compd.* **2019**, *791*, 1015–1024. [CrossRef]
34. GmbH, M. *Engine Testing, Pistons and Engine Testing*; Springer: Berlin/Heidelberg, Germany, 2012; pp. 115–280.
35. Ino, N. Fivefold twinned particles. *J. Phys. Soc. Jpn.* **1969**, *27*, 941–953. [CrossRef]

36. Tiryakioğlu, M. Si particle size and aspect ratio distributions in an Al–7% Si–0.6% Mg alloy during solution treatment. *Mater. Sci. Eng. A* **2008**, *473*, 1–6.
37. Han, W.; Cheng, G.; Li, S.; Wu, S.; Zhang, Z. Deformation induced microtwins and stacking faults in aluminum single crystal. *Phys. Rev. Lett.* **2008**, *101*, 115505. [CrossRef]
38. Chen, M.; Ma, E.; Hemker, K.J.; Sheng, H.; Wang, Y.; Cheng, X. Deformation twinning in nanocrystalline aluminum. *Science* **2003**, *300*, 1275–1277. [CrossRef]
39. Chen, G.; Zhang, W.; Iizuka, T. The fatigue fracture characteristics of the bond zone of aluminum matrix composites (Al-12Si/ABOw) with Al-12Si alloys. *Mater. Sci. Eng. A* **2019**, *755*, 181–189.
40. Dezecot, S.; Maurel, V.; Buffiere, J.-Y.; Szmytka, F.; Koster, A. 3D characterization and modeling of low cycle fatigue damage mechanisms at high temperature in a cast aluminum alloy. *Acta Mater.* **2017**, *123*, 24–34. [CrossRef]
41. Shaha, S.; Czerwinski, F.; Kasprzak, W.; Chen, D. Tensile and compressive deformation behavior of the Al–Si–Cu–Mg cast alloy with additions of Zr, V and Ti. *Mater. Des.* **2014**, *59*, 352–358. [CrossRef]

Disclaimer/Publisher's Note: The statements, opinions and data contained in all publications are solely those of the individual author(s) and contributor(s) and not of MDPI and/or the editor(s). MDPI and/or the editor(s) disclaim responsibility for any injury to people or property resulting from any ideas, methods, instructions or products referred to in the content.